Progress in Photovoltaics: Research and Applications

WILEY

PROGRESS IN PHOTOVOLTAICS

RESEARCH ARTICLE OPEN ACCESS

Exploring the Synthesis of $Cu_2(Zn,Cd)SnS_4$ at High Temperatures as a Route for High-Efficiency Solar Cells

Outman El Khouja[1,2] | Yuancai Gong[3,4] | Alex Jimenez-Arguijo[3,4] | Maykel Jimenez Guerra[3,4] | Axel Gon Medaille[3,4] | Romain Scaffidi[5,6,7,8] | Arindam Basak[9] | Cristian Radu[1,10] | Denis Flandre[5,6,7,8] | Bart Vermang[5,6,7,8] | Sergio Giraldo[3,4] | Marcel Placidi[3,4] | Zacharie Jehl Li-Kao[3,4] | Aurelian Catalin Galca[1,11] | Edgardo Saucedo[3,4]

[1]National Institute of Materials Physics, Magurele, Ilfov, Romania | [2]Faculty of Science, Ibn Tofail University, Campus Universitaire, Kenitra, Morocco | [3]Universitat Politècnica de Catalunya (UPC), Barcelona, Spain | [4]Barcelona Centre for Multiscale Science & Engineering, Universitat Politècnica de Catalunya (UPC), Barcelona, Spain | [5]IMO, Hasselt University, Diepenbeek, Belgium | [6]IMOMEC, imec, Diepenbeek, Belgium | [7]EnergyVille 2, Genk, Belgium | [8]ICTEAM, UCLouvain, Louvain-la-Neuve, Belgium | [9]Thin Film Photovoltaic Lab, School of Electronics Engineering, KIIT-Deemed to Be University, Bhubaneswar, India | [10]Faculty of Physics, University of Bucharest, Magurele, Ilfov, Romania | [11]International Centre for Advanced Training and Research in Physics, Magurele, Ilfov, Romania

Correspondence: Aurelian Catalin Galca (ac_galca@infim.ro) | Edgardo Saucedo (edgardo.saucedo@upc.edu)

Received: 30 July 2024 | **Revised:** 12 December 2024 | **Accepted:** 4 February 2025

Funding: NIMP authors acknowledge funding from *Ministerul Cercetării, Inovării și Digitalizării* (Romanian Ministry of Research, Innovation and Digitalization) through the Core Programme PC3-PN23080303 project, and from *Unitatea Executivă pentru Finanțarea Învățământului Superior, a Cercetării, Dezvoltării și Inovării* (UEFISCDI) through PN–III–P4-ID-PCE-2020-0827 (Contract no. PCE74 09/02/2021) and ERANET-M-3-ERANET-Ligthcell (Contract No. 19/15.03.2024) projects. Authors acknowledge the COST Action Research and International Networking project "Emerging Inorganic Chalcogenides for Photovoltaics (RENEW-PV)," CA21148, supported by COST (European Cooperation in Science and Technology). This work received also funding from the European Union's Horizon 2020 research and innovation program under grant agreement number 952982 (CUSTOM-ART) and 866018 (SENSATE), and by the Science Ministry of Spain (*Ministerio de Ciencia, Innovación y Universidades*) projects number PID2020-116719RB-C41 (MATER-ONE) and TED2021-130265B-C21 (MIRACLE). A. J. A. thanks the European Social Fund+ for the FI fellowship. S.G. thanks the Juan de la Cierva grant IJC2020-044716-I funded by *Ministerio de Ciencia, Innovación y Universidades* (MCIN/AEI/10.13039/501100011033) and by European Union's Horizon 2020 research and innovation program, NextGenerationEU/PRTR. E. S. is grateful to ICREA (*Institució Catalana de Recerca i Estudis Avançats*) Academia program. R. S. thanks *Fonds Wetenschappelijk Onderzoek* (FWO) for the funding through the Fundamental Research PhD Fellowship (1178024N). A. B. thanks the grant SIR/2022/001011 by Science and Engineering Research Board (SERB) India. Horizon 2020 Framework Programme.

Keywords: CZCTS films | photovoltaic optimization | structural characterization | sulfurization temperature tuning

ABSTRACT

The present research explores for the first time the intricate relationship between sulfurization temperature at unusual high temperatures (up to 700°C) and the structural/optoelectronic properties of $Cu_2(Zn,Cd)SnS_4$ (CZCTS) thin films, synthesized via a two-step sequential process involving the precursor film deposition using aprotic molecular ink followed by thermal treatment in sulfur atmosphere. X-ray diffraction patterns confirms the tetragonal structure. Scanning Electron Micrographs revealed significant grain growth, with grain sizes increasing from ~0.3 μm at 620°C to ~1.5 μm at 680°C, effectively reducing grain boundary recombination. Energy dispersive X-ray spectroscopy demonstrated a Cu-poor and Zn-rich composition, with a consistent Cd incorporation of ~3.7 at%. Raman spectroscopy showcases the homogeneity and purity of the CZCTS crystalline structure. Precise control of the sulfurization temperature plays a crucial role in determining the photovoltaic characteristics of CZCTS-based solar cells. By increasing the grain size and preventing the thermal decomposition of the CZTS phase, the photovoltaic performance peaked at a sulfurization temperature of 680°C, achieving a power conversion efficiency (PCE) of 10.4%, with an open-circuit voltage of 0.701 V, a short-circuit current density of 24.3 mA/cm^2 and a fill factor of 60.8%. External quantum efficiency reached a maximum of 83.3% at 580 nm. The bandgap of the CZCTS absorber was determined to be 1.48 eV, optimal for

photovoltaic applications. However, further increasing the sulfurization temperature to 700°C resulted in a lower PCE of 8.5%, attributed to interface degradation and secondary phase formation. Temperature-dependent current–voltage measurements revealed a reduction in recombination losses, with an activation energy of 1.24 eV at the CZCTS/CdS interface, indicating effective defect passivation by Cd incorporation. The optimized films, sulfurized at 680°C, displayed an absorber thickness of ~1.2 μm after sulfurization, providing efficient light absorption and charge transport. The findings not only emphasize the critical role of sulfurization temperature in engineering CZCTS film and subsequently their functionality but also provide valuable insights for fine tuning their performance in the field of photovoltaic applications.

1 | Introduction

Emerging renewable energy sources present a pioneering solution to mitigate the challenges posed by the energy crisis and environmental pollution. Among these, photovoltaic power generation technology emerges as a practical and vital cornerstone for realizing sustainable environmental conservation, energy efficiency, and emission reduction. This innovative approach not only addresses the pressing need for cleaner energy alternatives but also shows a significant leap toward fostering a green, sustainable future [1, 2]. Copper zinc tin sulfoselenide (CZTSSe) solar cells, based on the kesterite crystal structure, stand out as one of the most promising emerging technologies in the realm of photovoltaics. Their exceptional potential in the third generation of solar technologies comes from a combination of factors, including earth-abundant materials, a tunable direct bandgap, high optical absorption coefficients, environmentally friendly characteristics, and a relatively cost-effectiveness. This convergence of properties positions CZTSSe solar cells as a formidable candidate, charting a course toward a sustainable and economically viable future of photovoltaic technologies [3–7]. CZTSSe solar cells, evolved from 2nd generation Cu(In,Ga)(S,Se)$_2$ (CIGS), mark a significant stride forward. It is noteworthy that the current pinnacle of power conversion efficiency (PCE) for CIGS devices stands at 23.35%, achieved through vacuum methods [8]. In contrast, CZTSSe devices have demonstrated competitive PCE values using solution processing techniques. The vacuum processes inherent to CIGS synthesis demand substantial energy inputs, considerable capital investment, and result in excessive operating costs. Furthermore, underlines the unique benefits of CZTSSe, which through solution processing not only yields encouraging results but also provides a more effective and economically viable alternative in the constantly changing field of solar cell technology [9]. Moreover, the translation of high-performance devices from laboratory settings to large-scale commercial production encounters challenges like low yields, process intricacies, and material utilization complexities. Fortunately, the solution method emerges as a promising way with vast developmental potential, characterized by its cost-effectiveness, straightforward large-area preparation, and reproducible PCE [10, 11]. In 2021, Xin's group achieved a remarkable PCE of 13.0% utilizing a dimethyl sulfoxide (DMSO)-based processing approach [12]. Meng et al. [13] demonstrated further improvements, achieving an efficiency of 13.6% through innovative solution methods, recently being reported an updated value of approximately 15% [14]. Significantly, the certified efficiency of CZTSSe solar cells fabricated using the solution method exceeded the highest efficiency of 12.62%, previously set by Kim et al. [15] using vacuum methods. This highlights the pivotal role of solution processing, not only in achieving competitive efficiencies but also in surpassing benchmarks established by traditional vacuum methods.

Currently, the production of CZTSSe absorbers through solution processing typically involves the following steps: (*i*) deposit of a precursor layer to the substrate and (*ii*) heat treatment of the precursor layer under sulfur and/or an inert atmosphere to produce the final polycrystalline absorbers [16]. While the highest efficiency recorded for CZTSSe solar cells manufactured through solution processing is at an impressive 14.9%, it is noteworthy that this figure still significantly lags behind the theoretical limit predicted by the Shockley–Queisser model, which stands at approximately 32%. The disparity highlights the existing gap between real-world achievements and the theoretical upper bounds within the field of CZTSSe solar cell efficiency. Subsequently, it emphasizes the significance of ongoing research and developments in fabrication techniques in order to bridge this gap and get closer to attaining the maximal efficiency potential predicted by the Shockley–Queisser model. The key to producing high-efficiency CZTSSe solar cells is getting top-tier absorber films [17, 18].

The utilization of a hydrazine-based precursor solution stands as the most successful method for CZTSSe solar cell preparation within the solution processing paradigm. This innovative approach, pioneered by IBM in 2010, achieved a groundbreaking certified conversion efficiency of 12.6% in 2013, a record efficiency that has set the standard for several years [19, 20]. Nevertheless, hydrazine solvents pose inherent challenges due to their highly toxic and explosive nature, coupled with explicit transportation and application restrictions in certain countries and regions. These limitations have catalyzed a rapid shift toward the development and widespread adoption of solution methods employing non-hydrazine solvent systems. Presently, an array of environmentally friendly, stable, and high-efficiency solvent systems has emerged. Notable examples include dimethyl sulfoxide (DMSO), N,N-dimethylformamide (DMF), ethylene glycol methyl ether (EGME), thioglycolic acid and ammonia (TGA), and the ethylenediamine/ethanedithiol system (EN/EDT). This transformative shift not only addresses safety concerns but also signifies a pivotal advancement in the field of CZTSSe solar cell fabrication, promoting sustainability and wider accessibility [21]. Table 1 displays a selected overview of the experimental settings and device performances of CZTS/CZTSSe based solar cells employing various solvent-based solution-deposited absorbers.

Reducing the significant V_{oc} losses found in kesterite solar cells has mainly depended on improving absorber qualities through techniques such controlling Cu-Zn disorder, reducing surface and grain boundary imperfections, and controlling absorber grain development [58–60]. Several studies have exhibited strategies to improve the absorber characteristics in kesterite solar cells. Extended low-temperature annealing enhances

TABLE 1 | Overview of the experimental settings and device performances of CZTS/CZTSSe based solar cells employing various solvent-based solution-deposited absorbers.

Solar cell	Molecular ink solvent	Dissolution condition	Heat treatments	V_{oc}	J_{sc}	FF	PCE	Ref.
CZTSSe	N_2H_4	N_2, glove box	500°C	513.4	35.2	69.8	12.6	Wang et al. (2014) [20]
CZTSSe	N_2H_4	N_2, glove box	500°C	471	37.1	70.3	12.7	Kim et al. (2014) [22]
CZTS	MOE and MEA	Stirring (50°C)	580°C	664	14.8	58	5.7	Zhang et al. (2014) [23]
CZTSSe	$C_6H_{15}N/C_3H_8S$	N_2, glove box	500°C	382	34.4	60.1	7.86	K. W. Brew et al. (2015) [24]
CZTS	MOE	Stirring (50°C)	250°C + 580°C	581	24.1	66	9.82	Z. Su et al. (2015) [25]
CZTSSe	DMSO	Stirring	540°C	449	38.8	68.1	11.8	Xin et al. (2015) [26]
CZTSSe	MOE	Stirring	560°C	446	32.22	55.97	8.04	Y.-T. Hsieh (2016) [27]
CZTSSe	TGA, CH_3NH_2	Stirred (45°C)	510°C	378	28.17	65.4	6.96	Y. Yang et al. (2016) [28]
CZTSSe	$C_2H_4(SH)_2$. and $C_2H_4(NH_2)_2$	Stirring (60°C)	480°C	448	35.19	65.66	10.36	Guchhait et al. (2017) [29]
CZTS	MOE	Stirring (50°C)	600°C	650	25	66.2	10.8	S. H. Hadke et al. (2018) [30]
CZTSSe	DMSO + Tu	Stirring	550°C	463	33.4	65.5	10.1	C. M. Sutter-Fella et al. (2018) [31]
CZTSSe	DMSO	Stirring	300°C, 500°C, 550°C	531	33.7	64.8	11.6	A. Cabas-Vidani et al. (2018) [32]
CZTSSe	EGME	Stirring	540°C + 520°C	578	30.5	63	11.1	S.-H. Wu et al. (2018) [33]
CZTSSe	$C_2H_4(SH)_2$. and $C_2H_4(NH_2)_2$	Stirring	550°C	386	29.36	57.26	6.49	Q. Yan et al. (2019) [34]
CZGTS	DMF	N_2, glove box	540°C	583	33.60	55.9	11.0	J. A. Clark et al. (2019) [35]
CZTSSe	DMSO	Stirring	560°C	460	32.2	58.2	8.6	S. Ge et al. (2019) [36]
CZTS	MOE	Stirring (60°C)	200°C + 580°C	640	27.8	71	12.6	Z. Su et al. (2020) [37]
CZTS	MOE	Stirring (50°C)	600°C	670	21.5	57.22	8.24	A. Ibrahim et al. (2020) [38]
CZTSSe	MOE	Stirring (60°C)	550°C	465.1	39.33	66.51	12.18	X. G. Zhao et al. (2020) [39]
CZTSSe	MOE	Stirring (60°C)	555°C	507	33.97	65.36	11.1	G.-X. Liang et al. (2021) [40]
CZTSSe	1 $C_2H_4(SH)_2$. and $C_2H_4(NH_2)_2$ + stabilizer	Stirring (70°C)	550°C	495	37.07	66.26	12.16	X. Chang et al. (2021) [41]

(Continues)

TABLE 1 | (Continued)

Solar cell	Molecular ink solvent	Dissolution condition	Heat treatments	V_{oc}	J_{sc}	FF	PCE	Ref.
CZTSSe	DMSO	N_2, glove box	550°C	540	32.1	72.3	12.5	Y. Gong et al. (2021) [42]
CZTSSe	$C_2H_4(SH)_2$. and $C_2H_4(NH_2)_2$	Stirring (70°C)	300°C + 550°C	463	35.65	62.47	10.24	W. Xie et al. (2022) [43]
CZTSSe	DMF/DMSO binary solvents	Stirring	530°C	493.5	33.89	73.30	12.26	Y. Sun et al. (2022) [44]
CZTSSe	DMF	Stirring	550°C	501	35.36	66.4	11.76	Y. Cui et al. (2022) [45]
CZTSSe	DMSO	N_2, glove box	550°C	529	33.7	72.9	13.0	Y. Gong et al. (2022) [12]
CZTSSe	MOE	Stirring (60°C)	550°C	505.5	39.3	64.8	12.87	H. Geng et al. (2022) [46]
CZTSSe	DMF	Stirring	550°C	520	39.08	63.32	12.86	M. Wang et al. (2023) [47]
CZCTS	DMSO	Stirring	625°C	640	27.8	71.0	12.3	X. Pan et al. (2023) [48]
CZTSSe	MOE	Stirring	550°C	526.1	36.37	66.52	13.02	Y. Qi et al. (2023) [49]
CZTSSe	MOE, DMSO, DMF	Stirring (60°C)	535 °C	551.20	35.74	71.73	13.8	J. Zhou et al. (2023) [50]
CZTSSe	$C_2H_4(SH)_2$. and $C_2H_4(NH_2)_2$	Stirring (55°C)	550°C	513.85	38.69	69.27	13.77	L. Cao et al. (2024) [51]
CZTSSe	DMF	Not mentioned	Not mentioned	471.7	34.98	73.61	12.15	J. Zhou et al. (2024) [52]
CZTSSe	MOE	Stirring	520°C	576.0	36.9	70.0	14.9	Y. Li et al. (2024) [53]
CZTSSe	MOE	Stirring	560°C	573.0	35.1	70.1	14.1	Y. Gong et al. (2024) [54]
CZTSSe	MOE	Stirring (50°C)	540°C	555	36.7	71.2	14.5	J. Wang et al. (2024) [55]
CZTSSe	MOE	Stirring	555°C	580	36.63	67.43	14.3	Y. Zhao et al. (2024) [56]
CZTS	MOE	Stirring (60°C)	620°C	664	24.28	62.33	10.0	F. Ye et al. (2024) [57]

Cu-Zn disorder and increases V_{oc} of the device. SnO_x is created by heat treatment in air, which passivates flaws at the grain boundaries and absorber surface and can achieve efficiencies of up to 12.6%. Grain growth is managed by carefully controlled sulfo-selenization processes, which improves device efficiency [15, 20, 61]. Cd alloying pure sulfide kesterite has an array of benefits, including stabilizing the conduction band offset, reducing Cu_{Zn} antisite defects, and positively modulating the bandgap [21, 37]. Through the use of several deposition processes, including co-evaporation and solution-based procedures, the incorporation of Cd has resulted in efficiency gains of up to 10% in CZTS solar cells. Notable improvements, such as over 12% efficiency in CZCTS solar cells, have been reported; these were made possible by interface defect elimination and post-annealing [37, 62]. High-efficiency CZCTS solar cells often require high-temperature post-annealing or CZTS/CdS heterojunction heat treatment [63]. The full potential of Cd alloying in CZCTS remains untapped. Recent findings reveal that defect cluster formation, impacting kesterite band tailing, is related to absorber grain growth mechanisms. Direct-phase transformation grain growth, facilitated by Cu^+-Sn^{4+}-based DMSO solutions, shows promise in suppressing defect formation [64]. This approach, successful in CZTSSe solar cells, holds the potential for enhancing CZCTS solar cell efficiency [12, 50].

This study explored, for the first time, the complex relationship between sulfurization at unusually high temperatures (up to 700°C) and the structural and optoelectronic characteristics

of Cd-based CZTS thin films. By fabricating CZTS absorbers using a Cu^{+}-Sn^{4+}-DMSO solution (supporting information [SI], Figure S1), the present study demonstrates the transformative impact of precise temperature control on the properties of the CZTS and corresponding device. Photovoltaic cells based on Cd free CZTS absorber layers crystallized at different temperatures had a maximum PCE of 4.08% and a V_{oc} of 576 mV (Figure S2 and Table S1). The analysis reveals that high sulfurization temperatures induce a transformation in crystallinity, driving the transition from an amorphous to a crystalline structure. This process is accompanied by significant grain growth, which effectively reduces band tailing and enhances the optoelectronic properties of the films. By introducing Cd in the CZTS, along with band gap decrease, the CdS/CZCTS interface change in positive manner the photovoltaic properties. As a result, the PCE increases, peaking at 10.4% at an optimal sulfurization temperature of 680°C, underscoring the critical role of grain boundary passivation and interface engineering. However, further increasing the sulfurization temperature to 700°C led to performance degradation, attributed to secondary phase formation and interface degradation, thus highlighting potential trade-offs in optimizing processing conditions. Importantly, the incorporation of 20% Cd into CZTS not only stabilized the conduction band offset but also significantly reduced the V_{oc} loss for CZCTS devices, even without post-heat treatment of the CZCTS/CdS heterojunction. This work establishes a novel approach for tuning kesterite-based thin films through a combination of Cd-alloying and sulfurization temperature optimization, providing valuable insights into achieving higher efficiencies and advancing the field of scalable, solution-processed photovoltaics.

2 | Materials and Methods

2.1 | Reagents and Materials

Dimethyl sulfoxide (DMSO), Thiourea (99%), CuCl (99.99%), $SnCl_4$ (99.998%), Zn $(Ac)_2$ (99.99%), and $CdCl_2$ (98%), all purchased from Sigma-Aldrich, have been used as chemicals.

2.2 | CZCTS Precursor Film Preparation

The precursor solution was prepared under ambient air condition, with all chemicals used as received without further purification. The 6 mmol of CuCl, 3 mmol of $SnCl_4$, 3.7 mmol of Zn $(Ac)_2$, 0.74 mmol of $CdCl_2$ (corresponding to 20% of the total Zn + Cd molar content), and 27 mmol of thiourea were dissolved in 10 mL of dimethyl sulfoxide (DMSO) and stirred until complete dissolution. The yellow and clear precursor solution was obtained after 2-h stirring. The fabrication process described involves the spin-coating of the aprotic molecular ink onto Mo/SiO_2/Glass substrate (Suzhou ShangYang Solar Technology Co.), followed by annealing (300°C) to produce CZCTS films. The two-step sequence (spin-coating and annealing process), is repeated seven times to achieve a precursor film with a thickness of approximately 1 μm (Figure S3). The sulfurization of precursor films was conducted in a tubular furnace under precisely controlled conditions. The process began with a temperature ramp-up at a rate of 10°C/min, leading to the target temperature, which ranged between 620°C and 700°C (Figure S4). Once the desired temperature was reached, the films were held at this temperature for 15 min to allow thorough sulfur incorporation and complete the reaction. The sulfurization process was carried out under atmospheric pressure within a dedicated graphite box containing sulfur pellets (0.1 g) as the source material. The graphite box was specifically designed to establish an optimal sulfur-rich environment, effectively reducing contamination risks while ensuring a uniform distribution of sulfur vapor. This setup facilitated consistent sulfur incorporation across the film, which is crucial for achieving homogeneity in the materials structural and compositional properties.

2.3 | Film Characterization

XRD patterns were collected using an X-ray diffractometer featuring Cu Kα as the radiation source (Empyrean, PANalytical). Raman spectra were obtained using a Raman spectrometer (Lab-RAM HR Evolution, HORIBA) with a 532 nm laser diode as the excitation source. Detailed scanning electron microscopy (SEM) images were captured on a Hitachi S4800 SEM, utilizing a 10 kV accelerating voltage. The microstructure and elemental distribution of the sulfurized films were analyzed using a JEOL-F200CF STEM equipped with an energy dispersive X-ray spectroscopy (EDS) system.

2.4 | Device Fabrication and Characterization

For the device fabrication, initially, a 50 nm-thick CdS buffer layer was deposited onto the sulfurized films (Figure S5) using the chemical bath deposition method. Following this, radio frequency sputtering was employed to deposit intrinsic ZnO (i-ZnO) and indium tin oxide (ITO) to form the essential window layer. Thermal evaporation of Silver (Ag) using mechanical masks completed the entire device. More details are presented in the SI. As mention in the introduction, the optimization of the device fabrication has been done on Cd-free CZTS solar cells, structural and photovoltaic properties being also revealed in the SI. The current density–voltage (J–V) curves were recorded using a Keithley 2400 Source Meter under simulated AM 1.5 sunlight at 100 mW cm^{-2}, calibrated with a Si reference cell (12.8% efficiency over an aperture area of 0.23 cm^2). EQE measurements were conducted using the Enlitech QE-R test system, employing calibrated Si and Ge diodes as references.

3 | Results and Discussion

The XRD patterns of precursor films subjected to varying sulfurization temperatures are presented in Figure 1a. Aside from the peak originating from Mo (*110* reflection, $2\theta = 40.5°$, ICDD PDF no. 00-004-0809), the films show peaks at approximately 28.4°, 32.92°, 47.13°, 56.05°, and 58.71°, which correspond to tetragonal CZTS *112*, *220* and *312* diffraction lines (ICDD PDF no. 04-015-7542). The absence of significant deviations in the diffraction pattern implies a high level of structural integrity and successful alignment with present fabrication objectives. Moreover, from the observed patterns, the crystallite size evolution as function of sulfurization temperature provide useful insights into the film production process (SI, Figure S6). The gradual increase of

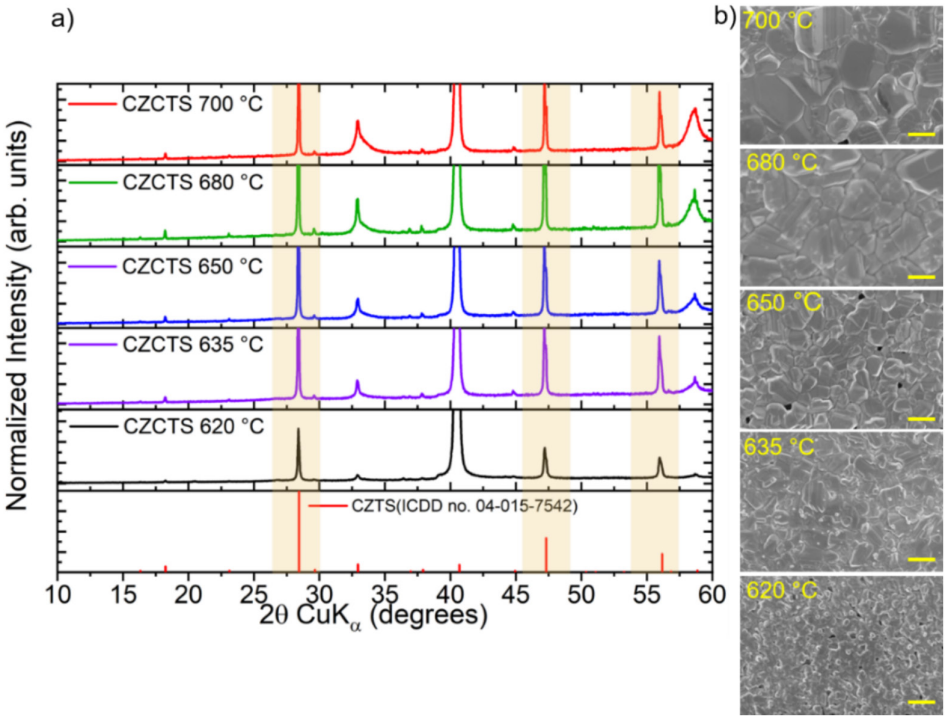

FIGURE 1 | (a) XRD and (b) SEM images of CZCTS thin films sulfurized at different temperature. All bars correspond to 1 μm (Mag = 10.00 KX).

the mean crystallite size (the coherence length along the crystallographic directions) up to 700°C shows a link between higher sulfurization temperatures and advantageous micro-crystallites formation. The subsequent decrease in crystallinity at 700°C implies the onset of adverse effects, potentially linked to decomposition processes. This nuanced relationship between sulfurization temperature and crystallinity points out the need for a well understanding of the thermal factors during the fabrication process.

The progressive increase in grain size with higher sulfurization temperatures (Figure 1b) indicates that elevated temperatures promote enhanced crystal growth and coalescence, leading to the formation of larger, well-defined grains within the CZCTS films, as shown in SEM images provided in the Figures 1b and S7. The improvement in grain morphology is vital for reducing grain boundary density, which directly impacts the performance of CZCTS-based solar cells. Grain boundaries are significant recombination centers, and their density directly influences the recombination rate. Since the recombination rate is proportional to the total grain boundary area, reducing the area inherently decreases recombination losses. This implies that the carrier lifetime at the grain boundaries is inversely proportional to the grain boundary area. Therefore, by promoting larger and more uniform grains, the total grain boundary area is minimized, leading to enhanced carrier lifetimes and better charge transport. This improvement translates into higher electrical conductivity and superior device efficiency. The SEM images reveal that at temperatures up to 680°C, the films exhibit compact and uniform grains, contributing to superior structural integrity and optoelectronic properties. However, at 700°C, pinholes become evident in the film, suggesting that excessive sulfurization temperatures may induce localized thermal decomposition

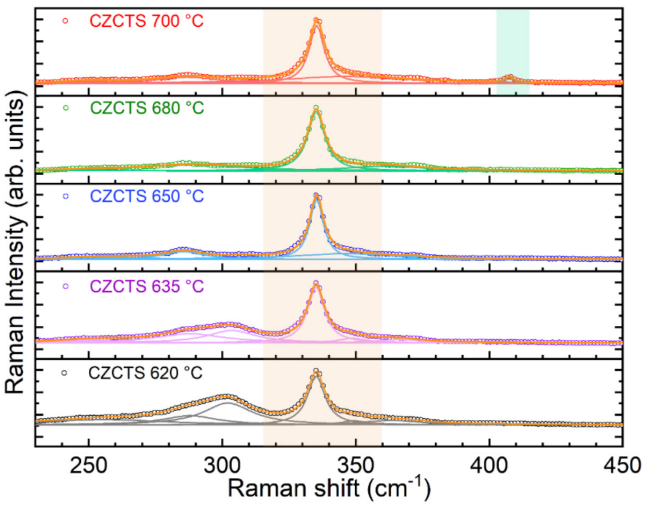

FIGURE 2 | Raman spectroscopy of CZCTS thin films.

or material defects, which compromise the film's quality. These observations align closely with the XRD results, where the increase in grain size observed in SEM correlates with the enhanced crystallite size and reduced lattice strain evident in the diffraction patterns. Thus, the complementary SEM and XRD analyses confirm that optimizing sulfurization temperature is critical to achieving the desired balance between improved crystallinity and minimal defect formation, thereby optimizing the CZCTS absorber's photovoltaic performance.

The Raman spectroscopy analysis of CZCTS films provides crucial insights into the structural characteristics of the material (Figure 2). The A1 vibration mode in the Raman spectra is

TABLE 2 | Raman shifts (cm^{-1}) corresponding to phonon modes identified from the Lorentzian components (shown in Figure 2) for the CZCTS films.

Row	CZCTS 620°C	CZCTS 635°C	CZCTS 650°C	CZCTS 680°C	CZCTS 700°C	Modes in KS phase	Atomic Movements	Experimental reported values
1	255.69	251.71	255.60	250.99	251.10	B $(TO)_{269}$	CZTS cations (Cu, Zn. Sn)||[001], against S	250 [65] 252 [66]
2	287.93	288.03	285.50	288.29	286.75	B $(LO)_{285}$	All cations||[001], against S	285 [66] 287 [67, 68] 288 [58, 69]
3	303.51	302.11	307.06	—	—	E $(TO)_{305}$ /A_{305}	Cu + Sn||[110], Cu + Zn||[1$\bar{1}$0]; net S contribution/S-only in the (*x*-*y*) plane	302 [70] 303 [58] 305 [71] 306 [66, 72]
4	335.16	335.10	335.06	335.15	335.37	A_{335} /B $(LO)_{335}$	S-only/Cu-Sn||[110], Cu + Zn||[1$\bar{1}$0]; net S contribution	334 [66] 335 [73] 336 [74] 337 [67, 75]
5	349.24	348.79	346.03	—	345.78	E $(LO)_{341}$	Zn||[110], Cu roughly opposite; two S against Zn and two other S against Cu	347 [66]
6	363.70	365.60	363.19	362.66		B $(TO)_{354}$	Cu-Zn||[001]; S in (*x*-*y*) plane	355 [76] 364 [77] 366 [65, 71] 367 [58]

observed as a dominant and well-defined peak at 335.6 cm^{-1}, which confirms the presence of the CZCTS kesterite crystal structure, validating the successful synthesis of the desired phase. The A1 mode is associated with S-only vibrations, with Cu-Sn and Cu-Zn vibrations against the [110] and [1–10] crystallographic directions, respectively, with a net sulfur contribution. The presence of the A1 mode across varying sulfurization temperatures indicates the stability of the CZCTS phase throughout the temperature range investigated, with minimal structural changes. Notably, there are no significant shifts or broadening in the A1 mode, suggesting that sulfurization up to 700°C does not induce notable thermal degradation or phase transitions, which is further corroborated by the XRD data showing stable crystallite sizes up to this temperature. Furthermore, at the higher sulfurization temperature of 700°C, an additional distinct peak emerges around 407 cm^{-1}, corresponding to the MoS_2 phase, which indicates the presence of this phase on or under the surface of the CZCTS, which might alter also the photovoltaic properties of the final device.

Table 2 summarizes values for distinctive modes within the KS phase of CZCTS films across a temperature spectrum (620°C to 700°C). Notably, B $(TO)_{269}$ characterizes CZTS cations aligning against S atoms||[001], with reported values spanning 250 to 252 cm^{-1}. B $(LO)_{285}$ signifies the alignment of all cations against S atoms||[001], exhibiting values from 285 cm^{-1} to 288 cm^{-1}. In E $(TO)_{305/A305}$, Cu + Sn aligns against [110], and Cu + Zn aligns against [11$\bar{0}$], involving a net sulfur contribution in the (x-y) plane, with reported values ranging from 302 to 306 cm^{-1}. A_{335}/B $(LO)_{335}$ captures S-only and cation vibrations against [110] and [11$\bar{0}$], respectively, with values in the range of 334 to 337 cm^{-1}. E $(LO)_{341}$ reveals Zn aligning against [110] with Cu oppositely positioned, incorporating specific S atoms against Zn and Cu, and reports values between 345 cm^{-1} and 349 cm^{-1}. B $(TO)_{354}$ features Cu-Zn alignment against [001] with S in the (*x*-*y*) plane, presenting values from 355 to 367 cm^{-1}.

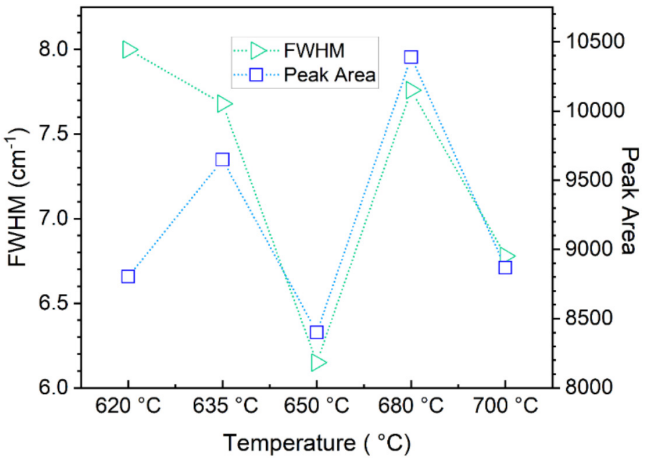

FIGURE 3 | FWHM and peak area of A_{335}/B $(LO)_{335}$ vibration mode of the CZCTS samples.

Across the temperature range, the Raman peak location of the A335/B (LO)335 mode is comparatively consistent, with a slight

larger Raman shift observed at 700°C. This trend is similar to what has been reported in other works investigating the temperature dependence of vibrational modes in CZTS and CZCTS films [58]. The number of active vibrational modes is represented by the area of the Raman peak, which increases typically with temperature. It reaches its maximum at 680°C and then starts to decrease slightly at 700°C. Up to 680°C, this trend suggests an improvement in crystalline quality or a decrease in defect density, consistent with observations from recent studies on the impact of temperature on CZTS crystallinity [78]. At higher temperatures, structural degradation or defect formation is likely, as indicated by the decrease in peak intensity and the broadening of the full width at half maximum (FWHM). The FWHM, an indication of crystalline quality that is inversely correlated, drops from 8.00 at 620°C to 6.15 at 650°C (Figure 3). Nonetheless, a minor rise in FWHM at 680°C and 700°C suggests that lattice strain or defect development may be beginning at these high temperatures. The intensity of the vibrational mode is represented by the height of the Raman peaks, which normally rise with temperature (the ratio A_{335}/B_{285} follows the same trend). The peak is reached around 650°C, and as temperatures rise, they gradually decrease. Up to 650°C, improvements in crystallinity are consistent with this pattern; at higher temperatures, there may be structural alterations or the introduction of defects.

Figure 4 shows the EDS coupled with SEM mapping, illustrating the uniform distribution of elements across the sample surface. The elemental composition (Table 3) confirms a desirable Cu-poor and Zn-rich profile in all films, which is known to favor enhanced photovoltaic performance by reducing deep-level defect states [79]. The Cd concentration remains consistent across all samples, while Zn content is similarly stable, supporting the

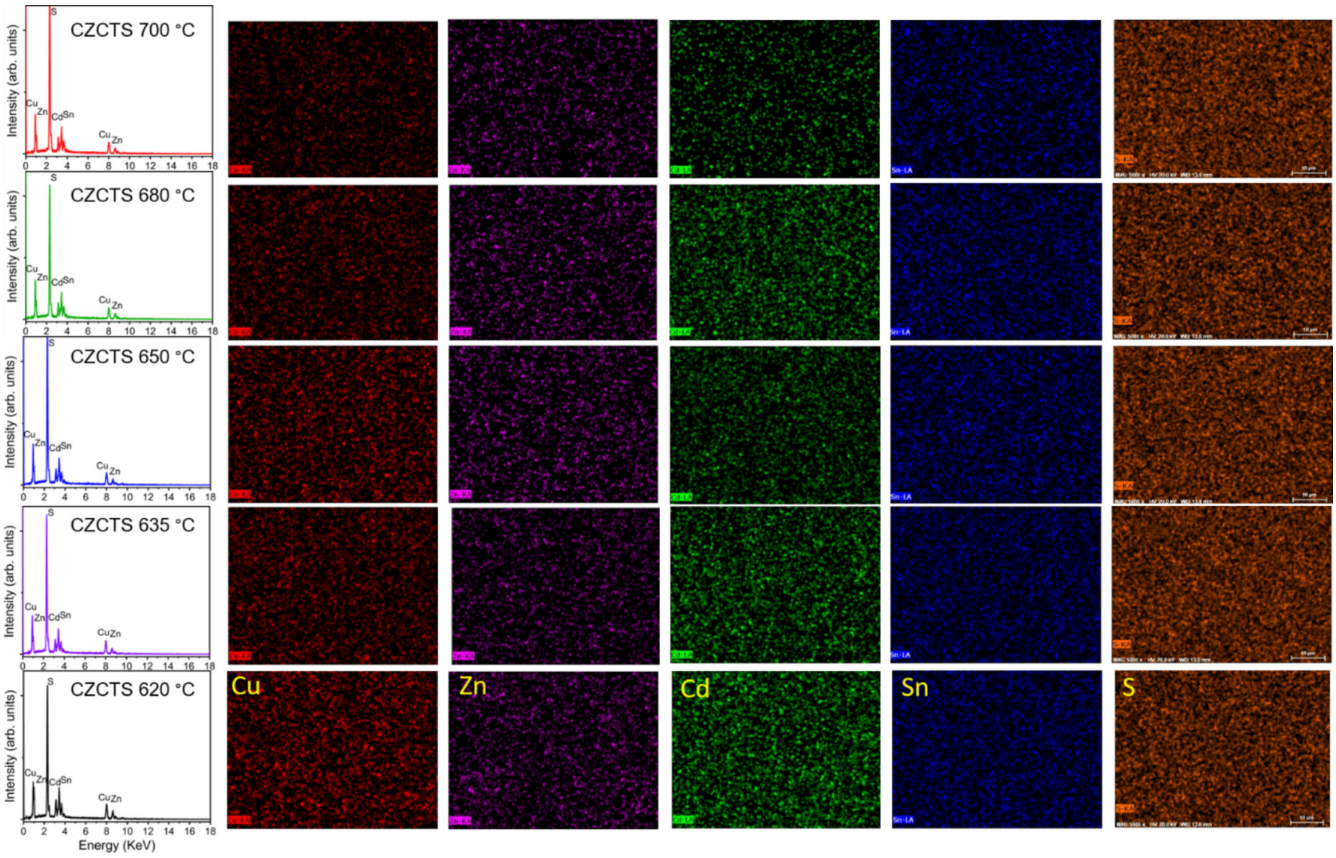

FIGURE 4 | EDS spectra, and the surface EDS mapping of the components elements of the sample sulfurized at different temperature.

TABLE 3 | Chemical elemental composition (at %) of the CZCTS films.

Sample	Cu (at.)	Zn (at.)	Cd (at.)	Sn (at.)	S (at)	Cu/(Zn + Cd + Sn)	(Zn + Cd)/Sn	S/cations
CZCTS 700°C	15.86	12.09	3.22	13.63	50.72	0.54	1.12	1.13
CZCTS 680°C	19.68	11.73	3.99	10.65	53.92	0.75	1.47	1.17
CZCTS 650°C	18.51	11.79	3.70	9.16	56.81	0.75	1.69	1.31
CZCTS 635°C	19.77	11.45	2.64	10.62	55.50	0.80	1.32	1.24
CZCTS 620°C	21.35	13.23	4.72	11.27	49.41	0.73	1.59	0.97

reproducibility of the alloying strategy. However, the tin concentration is relatively lower at lower sulfurization temperatures (620°C), while the sulfur content is also less at these temperatures, reaching a minimum at 635°C. Interestingly, at the highest sulfurization temperature (700°C), the Cu/(Zn + Cd + Sn) ratio decreases significantly to approximately 0.5, reflecting pronounced Cu depletion and unexpectedly high Sn concentrations. This anomalous composition at 700°C, which is typified by an excess of Sn and a Cu deficiency, may contribute to the lower performance in these samples. At higher temperatures, one might normally predict Sn loss through diffusion toward the surface following the evaporation, while the evaporated Sn is reabsorbed on the CZCTS surface considering the closed space feature of the graphite box. Alternatively, Cu may migrate to the MoS_2/Mo interface, as suggested by evidence from similar systems, driven by thermodynamic favorability or interfacial stabilization. This migration could also alter the stoichiometry and account for the Cu deficiency.

The performance of CZCTS based photovoltaic devices (Figure 5), as detailed in Table 4, reveals a well-defined trend with respect to sulfurization temperature. Starting at 620°C, the achieved PCE was 5.14%, accompanied by an open-circuit voltage (V_{oc}) of 0.480 V, a short-circuit current density (J_{sc}) of 18.97 mA cm^{-2}, and a fill factor (FF) of 56.75%. Subsequently, increasing the sulfurization temperature to 635°C resulted in an improved PCE of 6.16%, driven by a V_{oc} of 0.608 V and a J_{sc} of 22.03 mA cm^{-2}, albeit a slightly reduced FF of 46.32%. As the temperature further rose to 650°C, the PCE continued increasing, reaching 7.12% with a V_{oc} of 0.608 V, J_{sc} of 19.79 mA cm^{-2}, and an improved FF of 59.32%. At 680°C, the device achieved the maximum performance, with a PCE of 10.4%, attributed to a combination of the highest V_{oc} of 0.701 V, a J_{sc} of 24.31 mA cm^{-2}, and an FF of 60.81%. However, at 700°C, the PCE declined to 8.51%, corresponding to a slight reduction in V_{oc} of 0.624 V, J_{sc} of 24.07 mA cm^{-2}, while maintaining a relatively high FF of 59.13%. This trend aligns with observations reported in recent studies, where optimal sulfurization temperatures improve grain growth, crystallinity, and defect passivation, contributing to enhanced device performance. For example, Pan et al. [48] observed a similar increase in PCE with higher sulfurization temperatures due to reduced grain boundary recombination, with diminishing returns at excessively high temperatures attributed to interface degradation and secondary phase formation. The obtained results corroborate these findings, particularly the strong correlation between larger grain size at 680°C and reduced recombination losses.

The decline in PCE at 700°C can be ascribed to a delicate equilibrium between the beneficial and detrimental effects of the sulfurization process on the CZCTS absorber film. While increasing sulfurization temperatures generally lead to improved crystallinity, grain size, and charge carrier mobility, pushing the limits to 700°C might induce adverse effects, such as interfacial decomposition, phase segregation, secondary phase formation, or defect generation, which compromise electronic properties and overall photovoltaic performance as similarly reported in previous studies [21, 80, 81]. Additionally, at higher temperatures, there is a likelihood of enhanced grain boundary recombination and increased surface roughness, negatively impacting the charge transport properties within the film. Therefore, the decline in PCE at 700°C shows the critical importance of carefully optimizing sulfurization temperatures, recognizing that exceeding a certain limit can introduce detrimental factors that offset the gains achieved at lower temperatures, emphasizing the nuanced balance required for maximizing the efficiency of CZCTS absorber films [21, 80, 81].

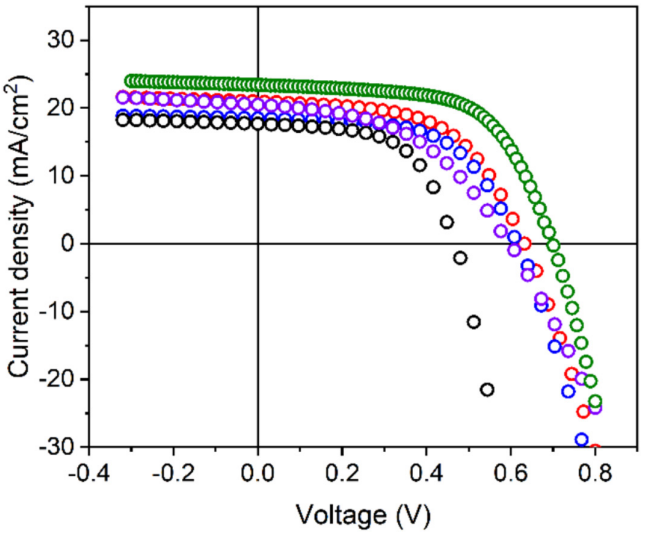

FIGURE 5 | *J–V* curves of CZCTS based devices.

TABLE 4 | Detailed parameters of photovoltaic devices based on the CZCTS films.

Sample	J_{sc} (mA/cm^2)	V_{oc} (mV)	FF (%)	PCE (%)
CZCTS 700°C	23.1	624	59.1	8.5
CZCTS 680°C	24.3	701	60.8	10.4
CZCTS 650°C	19.8	608	59.3	7.1
CZCTS 635°C	22.0	608	46.3	6.2
CZCTS 620°C	18.8	480	56.7	5.1

The cross-sectional SEM images depicted in Figure 6 offer insights into both the absorber and the devices engineered from the high-performance CZCTS films, prepared at 680°C. Notably, the images showcase a typical large-grain structure, with certain grains extending seamlessly throughout the entire thickness of the CZCTS layer. The strategic presence of such large grains holds intrinsic benefits for device performance, effectively minimizing the likelihood of recombination of photogenerated carriers at grain boundaries. This inherent characteristic demonstrates the potential of CZCTS films synthesized

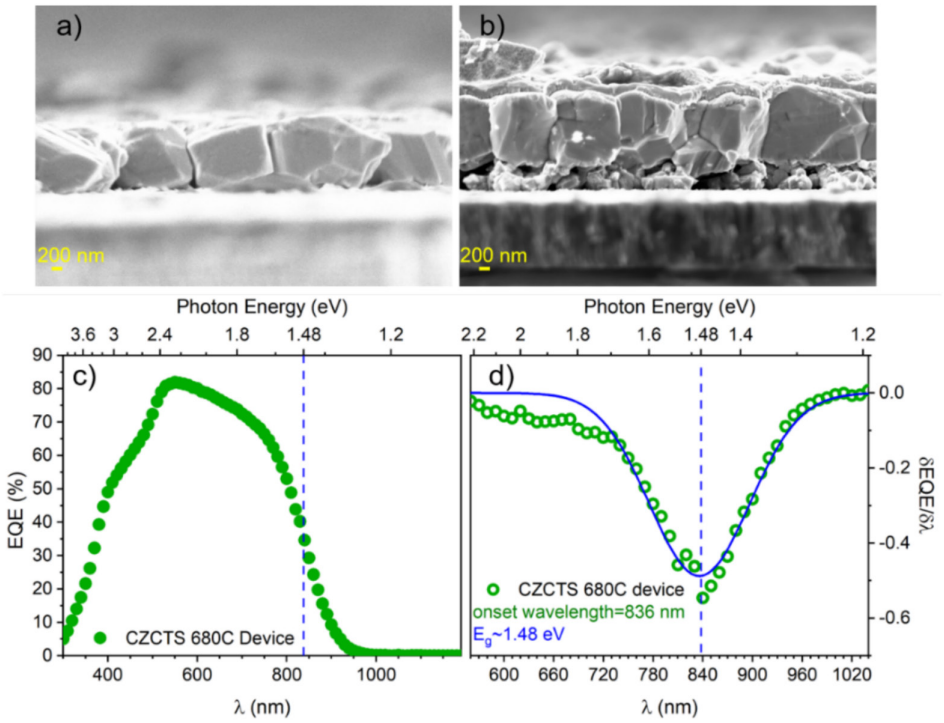

FIGURE 6 | Cross-section images of (a) the absorber layer, (b) the devices fabricated using CZCTS films sulfurized at 680°C, (c) EQE curve for the highest efficiency CZCTS device, and (d) the bandgap extracted from the inflection of the EQE curve.

at 680°C, highlighting their capacity to facilitate superior charge transport and collection within the photovoltaic device.

Figure 6c illustrates the external quantum efficiency (EQE) curve for the best device fabricated under standard conditions. The EQE spectra underscore the device commendable carrier collection efficiency, particularly in the near-infrared range, which is a crucial indicator of the absorber's quality and the device's internal charge transport properties. Notably, the EQE curve exhibits over 80% quantum efficiency across the entire visible light spectrum, peaking at 83.3% at a wavelength of 580 nm. This performance is comparable to or exceeds that reported in previous studies on CZTS and Cd-alloyed CZTS absorbers, where typical EQE values peak between 75% and 85% for devices fabricated using optimized conditions [78]. The obtained high quantum efficiency serves as a proof of the exceptional quality of the CZCTS absorber and the efficiency of charge carrier transport mechanisms within the device [82–84]. The current density, derived from the EQE data, is found to be 25.07 mA·cm^{-2}, which is in close agreement with values typically observed in high-performance CZTS-based devices. The obtained results in an active area efficiency of 10.4%, which is in line with, and sometimes surpasses, efficiencies seen in recent studies of Cd-alloyed CZTS devices processed under similar conditions. Discrepancies between the measured and EQE-integrated current density are attributed to suboptimal mask design and metal contact grids [82, 84]. Furthermore, from the EQE data is estimated the bandgap of the CZCTS absorber material of 1.48 eV (Figure 6d).

The substitution of Zn by Cd in CZTS absorbers plays a crucial role in altering the valence band (VB) and conduction band (CB) positions, significantly influencing the band alignment at the absorber/buffer heterojunction [85]. This modification is essential for optimizing the valence band offset (VBO) and conduction band offset (CBO), which dictate carrier transport and recombination dynamics at the interface. For heterojunction solar cells, an ideal band alignment involves a slightly positive CBO, forming a spike-like configuration that balances efficient carrier transport with minimized recombination losses. Theoretical studies, such as those by Minemoto et al. [86], have shown that CBO values between 0 and 0.4 eV are optimal for high-efficiency devices, particularly in CIGS cells. In the case of CZTS/CdS heterojunctions, experimental values of CBO vary widely but typically range from −0.34 eV (cliff-like, detrimental to efficiency) to +0.41 eV (spike-like, beneficial for performance). Haight et al. [87] reported a positive CBO of +0.41 eV, highlighting the potential of spike-like alignments to enhance charge collection and reduce recombination. Recently, Su et al. [37] achieved an optimal near-flat band CBO of +0.05 eV through Cd incorporation and post-deposition annealing, leading to an impressive, albeit non-certified, efficiency of 12.6%. These findings underscore a clear trend: low-efficiency cells often exhibit highly negative CBO values, which amplify recombination losses, whereas high-efficiency devices are associated with near-flat or slightly positive CBO values. This study highlights the importance of Cd incorporation and precise thermal annealing to fine-tune the electronic properties of CZTS. Adjusting these parameters is expected to yield a spike-like band alignment at the CZTS/CdS heterojunction, enhancing charge carrier separation, minimizing recombination, and ultimately improving device efficiency. By aligning the CBO within the ideal range, the proposed approach aims to bridge the gap between current and state-of-the-art performance in CZTS-based solar cells.

The energy band diagram (Figure S8) illustrates a spike-like CBO at the CZCTS/CdS interface. While sulfide-CZTS/CdS junctions typically exhibit a cliff-like CBO, the incorporation of Cd in CZCTS reduces this misalignment, bringing the CBO closer to optimal values for balancing efficient carrier transport and minimizing recombination losses. This improved band alignment prevents significant electron backflow into the absorber while facilitating smoother electron transfer into the CdS layer. The wide bandgap of CdS (~2.4 eV) not only enhances optical transparency, allowing more light to reach the absorber, but also plays a critical role in reducing recombination within the SCR. Furthermore, the band bending observed in the QNR of CZCTS supports effective charge separation by creating a strong electric field, driving photogenerated carriers toward the junction. These features, combined with the effects of Cd incorporation in modifying the band structure, highlight the critical role of both material composition and interface engineering in achieving improved photovoltaic performance.

The Urbach energy, as determined from the EQE analysis (Figure S9) E_u of 21 meV for the CZCTS device sulfurized at 680°C, indicating moderate suppression of band tailing states, which are caused by bandgap fluctuations due to compositional inhomogeneity and electrostatic potential fluctuations from deep-level defects. This relatively low E_u reflects reduced structural and compositional disorder, enhancing charge carrier transport and minimizing recombination losses, which are critical for improving photovoltaic performance. The presence of Cd in the sample contributes to this suppression of band tailing, as Cd alloying is known to reduce E_u by mitigating Cu/Zn disorder and passivating Sn-related defects [88]. The sulfurization temperature of 680°C appears to balance disorder suppression and defect formation, whereas higher temperatures, such as 700°C, are known to increase disorder through Cu depletion and secondary phase formation. These results emphasize the effectiveness of Cd alloying in reducing E_u and suggest further potential for defect passivation and precise thermal processing to optimize device efficiency.

To comprehensively investigate the impact of CZCTS properties on defect characteristics, temperature-dependent current–voltage (J–V) curves were conducted on CZCTS 680°C devices across a range of temperatures from 330 to 180 K, under standard solar intensity. The resulting temperature-dependent open-circuit voltage (V_{oc}-T) curves being illustrated in Figure 7, reveal critical insights into the device's recombination mechanisms. The higher current density of the CZCTS device is attributed to its lower bandgap (E_g = 1.48 eV), consistent with the expected trends in Cd-alloyed kesterite materials [89]. Furthermore, the sustained high current density at lower temperatures signifies a substantial reduction in charge carrier recombination within the absorber bulk, indicating that Cd alloying effectively suppresses the formation of deep-level defects [90, 91].

By extrapolating the linear segment of the V_{oc}-T curve, the activation energy (E_a) of the CZCTS device was determined to be 1.24 eV, yielding an E_a/E_g ratio of approximately 84%. This ratio is typically associated with recombination dominated at the heterojunction interface, as supported by recent studies on kesterite solar cells [92]. The E_a/E_g value is ≈84%, which is typically associated with limiting recombination dominated at

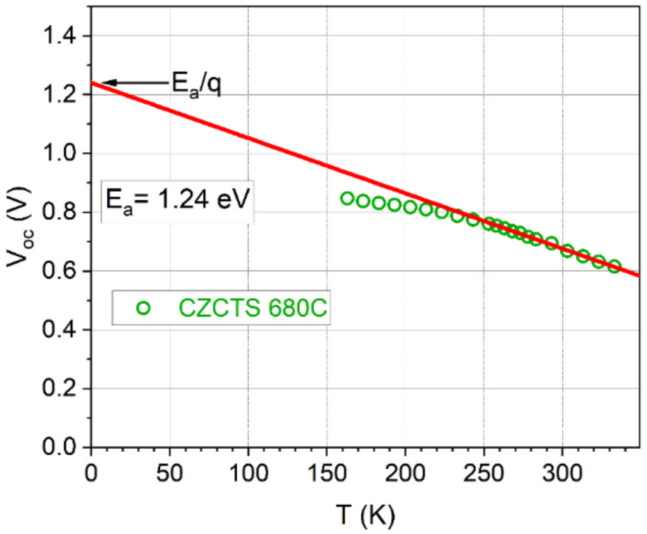

FIGURE 7 | Temperature dependence and linear extrapolation of V_{oc}. The 0 K intercept of the extrapolation is defined as activation energy E_a.

the heterojunction interface [92]. In this case, the high E_a/E_g value suggests that the Cd alloying has practically minimized the recombination at the heterojunction interface, leading to improved device performance and efficiency. The reduction in interface recombination due to Cd alloying can be attributed to several factors. First, Cd alloying can prevent Fermi-level pinning, which effectively reduces the recombination at the heterojunction interface [90]. Additionally, the alloying process can enhance charge carrier collection, thereby improving the overall device performance. Moreover, the effective reduction in the density of states at the heterojunction interface, as indicated by the high E_a/E_g ratio, enhances charge carrier transport and minimizes interface recombination, further boosting device efficiency [93]. These combined effects are in agreement with recent literature, which underscores the critical role of alloying strategies in optimizing heterojunction properties for high-performance solar cells [93]. The role of precise Cd alloying control in CZCTS absorbers significantly influences bulk and interface recombination mechanisms, offering key insights into improving efficiency and performance of kesterite-based solar cell devices.

The structural and compositional analysis of the CZCTS thin films and their interfaces were performed using various advanced microscopy techniques. A low magnification Transmission Electron Microscopy (TEM) image (Figure 8a) reveals the overall cell structure, highlighting the large grain size of the CZCTS 680°C layer. High-resolution TEM (HRTEM) images provide additional microstructural details, showing that the CZCTS grains are not uniformly oriented throughout the film, with some regions exhibiting crystal twinning. The twin boundaries observed in the HRTEM images traverse entire grains, indicating significant internal structural features (Figure 8b). The selected area electron diffraction (SAED) patterns taken from the CZCTS film confirm the crystalline nature of these grains, with the regions separated by the twinning boundary displaying the same zone axis but rotated relative to each other by approximately 109.4°, with a shared plane of (–112)/(1–12) (Figure 8A–C). At the interface between the CZCTS and CdS

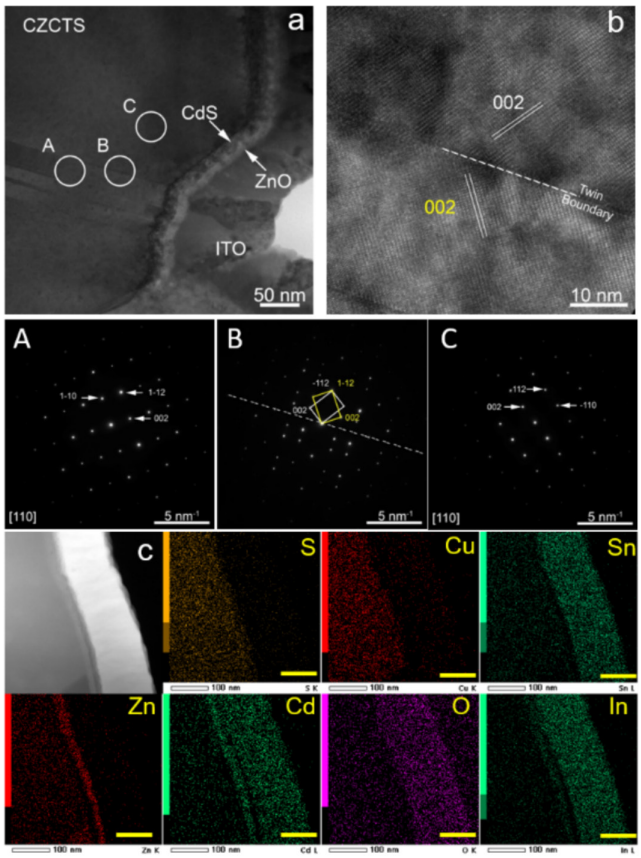

FIGURE 8 | (a) TEM cross-section image and (b) high-resolution transmission electron microscopy technique combined with fast Fourier transform, and energy dispersive X-ray spectroscopy mapping. The mapping bars correspond to 100 nm.

layers, the HRTEM and FFT analyses reveal a good crystallographic relationship, with the [001] axis of CZCTS parallel to the [001] axis of CdS. This alignment suggests a coherent interface, which is crucial for efficient charge transport, and minimizing recombination losses in solar cell. The Fourier images and simulations of diffraction patterns for both phases along the [010] zone axis confirm this crystallographic coherence.

Elemental mapping using scanning transmission electron microscopy (STEM) and energy dispersive X-ray spectroscopy (EDS) shows a uniform distribution of Cu, Zn, Sn, S, and Cd throughout the absorber layer, particularly highlighting the successful diffusion and reaction of Cd during the high-temperature sulfurization process (Figure 8c). The uniform distribution is crucial for maintaining the electronic properties of the absorber. Notably, secondary phases, often observed as ZnS, are identified at the upper and lower interfaces of the CZCTS layer. However, the distinct elemental distribution patterns suggest these phases may include $Zn_xCd_{1-x}S$ compounds rather than pure ZnS. The consistent intermixing of elements, delineated by the dashed yellow lines in the elemental maps, indicates a well-mixed interfacial region, which is beneficial for device performance.

Local HRTEM images and corresponding FFT patterns further validate the high crystallinity of the CZCTS absorber, as evidenced by the straight, parallel lattice planes and bright spots in the FFT patterns [49]. The measured lattice fringes correspond to an interplanar spacing of 0.328 nm, matching with the *112* reflection of kesterite CZTS crystals, corroborating the XRD findings [6, 94]. Compared to recent reports, the obtained results confirm structural and compositional stability of the CZCTS layer, even under high-temperature sulfurization, while emphasizing the critical balance between grain growth, secondary phase formation, and interfacial quality to enhance device optimization and reliability.

It's worth mentioning that TEM analysis revealed that MoS_2 forms at the CZCTS/Mo interface during high-temperature sulfurization. In the same time voids are present which can act as rear contact passivation layers while the remaining contacts will collect the charges and will keep in the same time a good adherence of the absorber films (Figure S10). Thus, CZCTS/Mo interface recombination is minimized. The result aligns with previous studies, such as the one by Vermang et al. [95], which emphasize the role of rear surface passivation in reducing recombination and improving device efficiency. The back contact chemical reactions as outlined by Scragg et al. [96]. lead to formation of gaseous phases which finally induces the voids present at CZCTS/Mo interface in the final devices. Liu et al. [97] demonstrates an effective method for fabricating highly efficient, ultrathin CZTS solar cells by controlling interfacial reactions using an Al_2O_3 intermediate layer at the Mo/CZTS interface. The Al_2O_3 layer prevents detrimental interfacial reactions during sulfurization, transforming into a self-organized nanopattern that reduces back contact recombination. This approach results in CZTS solar cells with efficiencies exceeding 8%, achieving world record efficiencies of 9.26% for small-area and 7.61% for standard CZTS solar cells. The formation of these passivation voids is beneficial in terms of reducing recombination at rear contact, without affecting the adherence of the films and the integrity of the final solar cells.

4 | Conclusion

The study highlights the pivotal role of sulfurization temperature in shaping the structural, optical, and photovoltaic properties of $Cu_2(ZnCd)SnS_4$ (CZCTS) thin films. Employing a two-step process of spin coating and precise thermal treatment, a high-quality tetragonal structure aligned with the desired Kesterite phase was achieved, as confirmed by X-ray diffraction and Raman spectroscopy. SEM imaging revealed a significant increase in grain size with elevated sulfurization temperatures, emphasizing the importance of temperature control for optimizing grain growth and minimizing recombination losses. The highest PCE of 10.4% was achieved at an optimal sulfurization temperature of 680°C, attributed to enhanced crystallinity, uniform Cd distribution, and suppressed deep defects. In contrast, sulfurization at 700°C led to a decrease in PCE, reflecting the onset of secondary phase formation and interfacial degradation. Cross-sectional SEM and high-resolution TEM analyses revealed deliberately engineered large-grain structures, complemented by elemental mapping that confirmed uniform Cd incorporation throughout the absorber layer. Structural improvements contributed to reduced carrier recombination and enhanced charge transport. The External quantum efficiency analysis demonstrated exceptional carrier collection efficiency,

peaking at 83.3% at 580 nm, while the estimated bandgap of 1.48 eV aligns well with the requirements for efficient light absorption in photovoltaic applications. The relatively lower efficiency (10.4%) of our CZCTS device, compared to state-of-the-art kesterite solar cells, is primarily limited by factors such as residual defects in the absorber layer, incomplete suppression of secondary phases, and non-optimal interfacial properties at the back contact and buffer layers. These challenges contribute to increased bulk and interface recombination, restricted charge carrier collection, and suboptimal band alignment. Additionally, the lack of advanced light-trapping designs and incomplete defect passivation may further limit the photogenerated current and voltage, ultimately constraining the PCE. Addressing these limitations requires comprehensive improvements across multiple fronts. Future research should focus on advanced defect passivation strategies, such as incorporating alkali elements (e.g., Na or K) to mitigate bulk defects and reduce recombination losses. Precise control of secondary phase formation during synthesis, combined with fine-tuning sulfurization conditions, can enhance crystallinity and grain size uniformity. Optimizing Cd alloying levels to achieve better band alignment and exploring alternative buffer layers, such as $Zn_{1-x}Sn_xO$ or TiO_2, could further improve interfacial charge transport properties. Investigating the alloying of elements such as Se or Ag, which can reduce defect formation energy and modulate the bandgap, as well as implementing light-trapping architectures or tandem designs, offers significant potential for further efficiency gains. Additionally, interface engineering approaches, such as introducing solid passivating layers like Al_2O_3, can suppress recombination at the back contact and enhance charge transport. These strategies form a strong foundation for the advancement of kesterite thin films and the optimization of CZCTS materials, accelerating the development of high-efficiency photovoltaic applications.

Acknowledgments

NIMP authors acknowledge funding from *Ministerul Cercetării, Inovării și Digitalizării* (Romanian Ministry of Research, Innovation and Digitalization) through the Core Programme PC3-PN23080303 project, and from *Unitatea Executivă pentru Finanțarea Învățământului Superior, a Cercetării, Dezvoltării și Inovării* (UEFISCDI) through PN–III–P4-ID-PCE-2020-0827 (Contract no. PCE74 09/02/2021) and ERANET-M-3-ERANET-Ligthcell (Contract No. 19/15.03.2024) projects. Authors acknowledge the COST Action Research and International Networking project "Emerging Inorganic Chalcogenides for Photovoltaics (RENEW-PV)," CA21148, supported by COST (European Cooperation in Science and Technology). This work received also funding from the European Union's Horizon 2020 research and innovation program under grant agreement number 952982 (CUSTOM-ART) and 866018 (SENSATE), and by the Science Ministry of Spain (*Ministerio de Ciencia, Innovación y Universidades*) projects number PID2020-116719RB-C41 (MATER-ONE) and TED2021-130265B-C21 (MIRACLE). A. J. A. thanks the European Social Fund+ for the FI fellowship. S.G. thanks the Juan de la Cierva grant IJC2020-044716-I funded by *Ministerio de Ciencia, Innovación y Universidades* (MCIN/AEI/10.13039/501100011033) and by European Union's Horizon 2020 research and innovation program, NextGenerationEU/PRTR. E. S. is grateful to ICREA (*Institució Catalana de Recerca i Estudis Avançats*) Academia program. R. S. thanks *Fonds Wetenschappelijk Onderzoek* (FWO) for the funding through the Fundamental Research PhD Fellowship (1178024N). A. B. thanks the grant SIR/2022/001011 by Science and Engineering Research Board (SERB) India. Open access publishing facilitated by Anelis Plus (the official name of "Asociatia Universitatilor, a Institutelor de Cercetare – Dezvoltare si a Bibliotecilor Centrale Universitare din Romania"), as part of the Wiley - Anelis Plus agreement.

Data Availability Statement

The data that support the findings of this study are available from the corresponding author upon reasonable request.

References

1. G. Liu, J. Xu, T. Chen, and K. Wang, "Progress in Thermoplasmonics for Solar Energy Applications," *Physics Reports* 981 (2022): 1–50, https://doi.org/10.1016/j.physrep.2022.07.002.

2. Y. M. Wei, K. Chen, J. N. Kang, W. Chen, X. Y. Wang, and X. Zhang, "Policy and Management of Carbon Peaking and Carbon Neutrality: A Literature Review," *Engineering* 14 (2022): 52–63, https://doi.org/10.1016/j.eng.2021.12.018.

3. M. A. Green, E. D. Dunlop, J. Hohl-Ebinger, et al., "Solar Cell Efficiency Tables (Version 60)," *Progress in Photovoltaics: Research and Applications* 30, no. 7 (2022): 687–701, https://doi.org/10.1002/pip.3595.

4. H. Zhou, W. C. Hsu, H. S. Duan, et al., "CZTS Nanocrystals: A Promising Approach for Next Generation Thin Film Photovoltaics," *Energy & Environmental Science* 6, no. 10 (2013): 2822–2838, https://doi.org/10.1039/c3ee41627e.

5. C. Wang, S. Chen, J. H. Yang, et al., "Design of I2-II-IV-VI4 Semiconductors Through Element Substitution: The Thermodynamic Stability Limit and Chemical Trend," *Chemistry of Materials* 26, no. 11 (2014): 3411–3417, https://doi.org/10.1021/cm500598x.

6. R. Fonoll-Rubio, J. Andrade-Arvizu, J. Blanco-Portals, et al., "Insights Into Interface and Bulk Defects in a High Efficiency Kesterite-Based Device," *Energy & Environmental Science* 14, no. 1 (2021): 507–523, https://doi.org/10.1039/d0ee02004d.

7. A. Polizzotti, I. L. Repins, R. Noufi, S. H. Wei, and D. B. Mitzi, "The State and Future Prospects of Kesterite Photovoltaics," *Energy & Environmental Science* 6, no. 11 (2013): 3171–3182, https://doi.org/10.1039/c3ee41781f.

8. Z. Xu, Q. Gao, C. Cui, et al., "Gradient Conduction Band Energy Engineering Driven High-Efficiency Solution-Processed Cu2ZnSn(S,Se)4/ZnxCd1–xS Solar Cells," *Advanced Functional Materials* 33, no. 3 (2023): 2209187, https://doi.org/10.1002/adfm.202209187.

9. Y. Cao, M. S. Denny, J. V. Caspar, et al., "High-Efficiency Solution-Processed Cu2ZnSn(S,Se)4 Thin-Film Solar Cells Prepared from Binary and Ternary Nanoparticles," *Journal of the American Chemical Society* 134, no. 38 (2012): 15644–15647, https://doi.org/10.1021/ja3057985.

10. S. Suresh and A. R. Uhl, "Present Status of Solution-Processing Routes for Cu (In,Ga)(S,Se)2 Solar Cell Absorbers," *Advanced Energy Materials* 11, no. 14 (2021): 2003743, https://doi.org/10.1002/aenm.202003743.

11. Y. Liu, B. Xu, X. Lu, et al., "Improvement of Grain Growth and Composition Distribution of Cu2ZnSn(S,Se)4 by Using Chloride-Based Precursor Solution," *Solar Energy* 215 (2021): 451–458, https://doi.org/10.1016/j.solener.2020.12.067.

12. Y. Gong, Q. Zhu, B. Li, et al., "Elemental De-Mixing-Induced Epitaxial Kesterite/CdS Interface Enabling 13%-Efficiency Kesterite Solar Cells," *Nature Energy* 7, no. 10 (2022): 966–977, https://doi.org/10.1038/s41560-022-01132-4.

13. M. Green, E. Dunlop, J. Hohl-Ebinger, M. Yoshita, N. Kopidakis, and X. Hao, "Solar Cell Efficiency Tables (Version 57)," *Progress in Photovoltaics: Research and Applications* 29, no. 1 (2021): 3–15, https://doi.org/10.1002/pip.3371.

14. M. A. Green, E. D. Dunlop, M. Yoshita, et al., "Solar Cell Efficiency Tables (Version 62)," *Progress in Photovoltaics: Research and Applications* 31, no. 7 (2023): 651–663, https://doi.org/10.1002/pip.3726.

15. D. H. Son, S. H. Kim, S. Y. Kim, et al., "Effect of Solid-H_2S gas Reactions on CZTSSe Thin Film Growth and Photovoltaic Properties of a 12.62% Efficiency Device," *Journal of Materials Chemistry A* 7, no. 44 (2019): 25279–25289, https://doi.org/10.1039/c9ta08310c.

16. S. Ge, H. Xu, S. N. Khan, et al., "A Universal and Facile Method of Tailoring the Thickness of Mo (Sx,Se1−x)2, Contributing to Highly Efficient Flexible Cu2ZnSn(S,Se)4 Solar Cells," *Solar RRL* 5, no. 10 (2021): 2100598, https://doi.org/10.1002/solr.202100598.

17. N. S. Arul, D. Y. Yun, D. U. Lee, and T. W. Kim, "Strong Quantum Confinement Effects in Kesterite Cu_2ZnSnS_4 Nanospheres for Organic Optoelectronic Cells," *Nanoscale* 5, no. 23 (2013): 11940–11943, https://doi.org/10.1039/c3nr03892k.

18. Z. Zhang, L. Yao, Y. Zhang, et al., "Modified Back Contact Interface of CZTSe Thin Film Solar Cells: Elimination of Double Layer Distribution in Absorber Layer," *Advancement of Science* 5, no. 2 (2018): 1700645, https://doi.org/10.1002/advs.201700645.

19. T. K. Todorov, K. B. Reuter, and D. B. Mitzi, "High-Efficiency Solar Cell With Earth-Abundant Liquid-Processed Absorber," *Advanced Materials* 22, no. 20 (2010): E156–E159, https://doi.org/10.1002/adma.200904155.

20. W. Wang, M. T. Winkler, O. Gunawan, et al., "Device Characteristics of CZTSSe Thin-Film Solar Cells With 12.6% Efficiency," *Advanced Energy Materials* 4, no. 7 (2014): 1301465, https://doi.org/10.1002/aenm.201301465.

21. L. Wang, Y. Wang, Z. Zhou, et al., "Progress and Prospectives of Solution-Processed Kesterite Absorbers for Photovoltaic Applications," *Nanoscale* 15, no. 20 (2023): 8900–8924, https://doi.org/10.1039/d3nr00218g.

22. J. Kim, H. Hiroi, T. K. Todorov, et al., "High Efficiency Cu2ZnSn(S,Se)4 Solar Cells by Applying a Double In2S3/CdS Emitter," *Advanced Materials* 26, no. 44 (2014): 7427–7431, https://doi.org/10.1002/adma.201402373.

23. K. Zhang, Z. Su, L. Zhao, et al., "Improving the Conversion Efficiency of Cu_2ZnSnS_4 Solar Cell by Low Pressure Sulfurization," *Applied Physics Letters* 104, no. 14 (2014): 141101, https://doi.org/10.1063/1.4870508.

24. K. W. Brew, S. M. McLeod, S. M. Garner, and R. Agrawal, "Improving Efficiencies of Cu_2ZnSnS_4 Nanoparticle Based Solar Cells on Flexible Glass Substrates," *Thin Solid Films* 642 (2017): 110–116, https://doi.org/10.1016/j.tsf.2017.09.009.

25. Z. Su, J. M. R. Tan, X. Li, X. Zeng, S. K. Batabyal, and L. H. Wong, "Cation Substitution of Solution-Processed Cu2ZnSnS4 Thin Film Solar Cell With Over 9% Efficiency," *Advanced Energy Materials* 5, no. 19 (2015): 1500682, https://doi.org/10.1002/aenm.201500682.

26. H. Xin, S. M. Vorpahl, A. D. Collord, et al., "Lithium-Doping Inverts the Nanoscale Electric Field at the Grain Boundaries in Cu2ZnSn(S,Se)4 and Increases Photovoltaic Efficiency," *Physical Chemistry Chemical Physics* 17, no. 37 (2015): 23859–23866, https://doi.org/10.1039/c5cp04707b.

27. Y. T. Hsieh, Q. Han, C. Jiang, et al., "Efficiency Enhancement of Cu2ZnSn(S,Se)4 Solar Cells via Alkali Metals Doping," *Advanced Energy Materials* 6, no. 7 (2016): 1502386, https://doi.org/10.1002/aenm.201502386.

28. Y. Yang, X. Kang, L. Huang, S. Wei, and D. Pan, "A General Water-Based Precursor Solution Approach to Deposit Earth Abundant Cu2ZnSn(S,Se)4 Thin Film Solar Cells," *Journal of Power Sources* 313 (2016): 15–20, https://doi.org/10.1016/j.jpowsour.2016.01.085.

29. A. Guchhait, Z. Su, Y. F. Tay, et al., "Enhancement of Open-Circuit Voltage of Solution-Processed Cu2ZnSnS4 Solar Cells With 7.2% Efficiency by Incorporation of Silver," *ACS Energy Letters* 1, no. 6 (2016): 1256–1261, https://doi.org/10.1021/acsenergylett.6b00509.

30. S. H. Hadke, S. Levcenko, S. Lie, et al., "Synergistic Effects of Double Cation Substitution in Solution-Processed CZTS Solar Cells With Over 10% Efficiency," *Advanced Energy Materials* 8, no. 32 (2018): 1802540, https://doi.org/10.1002/aenm.201802540.

31. C. M. Sutter-Fella, J. A. Stückelberger, H. Hagendorfer, et al., "Sodium Assisted Sintering of Chalcogenides and Its Application to Solution Processed Cu2ZnSn(S,Se)4 Thin Film Solar Cells," *Chemistry of Materials* 26, no. 3 (2014): 1420–1425, https://doi.org/10.1021/cm403504u.

32. A. Cabas-Vidani, S. G. Haass, C. Andres, et al., "High-Efficiency (LixCu1−x)2ZnSn(S,Se)4 Kesterite Solar Cells with Lithium Alloying," *Advanced Energy Materials* 8, no. 34 (2018): 1801191, https://doi.org/10.1002/aenm.201801191.

33. S. H. Wu, K. T. Huang, H. J. Chen, and C. F. Shih, "$Cu_2ZnSn(S_xSe_{1-x})_4$ Thin Film Solar Cell With High Sulfur Content (X Approximately 0.4) and Low Voc Deficit Prepared Using a Postsulfurization Process," *Solar Energy Materials & Solar Cells* 175 (2018): 89–95, https://doi.org/10.1016/j.solmat.2017.09.036.

34. Q. Yan, S. Cheng, X. Yu, et al., "Mechanism of Current Shunting in Flexible Cu2Zn1−xCdxSn(S,Se)4 Solar Cells," *Solar RRL* 4, no. 1 (2020): 1900410, https://doi.org/10.1002/solr.201900410.

35. J. A. Clark, A. Murray, J. M. Lee, T. S. Autrey, A. D. Collord, and H. W. Hillhouse, "Complexation Chemistry in N,N-Dimethylformamide-Based Molecular Inks for Chalcogenide Semiconductors and Photovoltaic Devices," *Journal of the American Chemical Society* 141, no. 1 (2019): 298–308, https://doi.org/10.1021/jacs.8b09966.

36. S. Ge, H. Gao, R. Hong, et al., "Improvement of Cu2ZnSn(S,Se)4 Solar Cells by Adding N,N-Dimethylformamide to the Dimethyl Sulfoxide-Based Precursor Ink," *ChemSusChem* 12, no. 8 (2019): 1692–1699, https://doi.org/10.1002/cssc.201803009.

37. Z. Su, G. Liang, P. Fan, et al., "Device Postannealing Enabling Over 12% Efficient Solution-Processed Cu2ZnSnS4 Solar Cells With Cd2+ Substitution," *Advanced Materials* 32, no. 32 (2020): 2000121, https://doi.org/10.1002/adma.202000121.

38. A. Ibrahim, A. Guchhait, S. Hadke, H. L. Seng, and L. H. Wong, "Silver and Potassium Incorporation in Double-Layer Solution-Processed Cu2ZnSnS4 Solar Cell," *ACS Applied Energy Materials* 3, no. 11 (2020): 10402–10407, https://doi.org/10.1021/acsaem.0c01165.

39. X. Zhao, Y. Pan, C. Zuo, et al., "Ambient Air-Processed Cu2ZnSn(S,Se)4 Solar Cells With Over 12% Efficiency," *Scientific Bulletin* 66, no. 9 (2021): 880–883, https://doi.org/10.1016/j.scib.2020.12.030.

40. G. X. Liang, Z. X. Yu, Z. G. Xie, et al., "Optimizing the Ratio of Sn4+ and Sn2+ in Cu2ZnSn(S,Se)4 Precursor Solution via Air Environment for Highly Efficient Solar Cells," *Solar RRL* 5, no. 11 (2021): 2100574, https://doi.org/10.1002/solr.202100574.

41. X. Chang, J. Fu, D. Kou, et al., "Synergistic Incorporation of NaF and CsF PDT for High Efficiency Kesterite Solar Cells: Unveiling of Grain Interior and Grain Boundary Effects," *Journal of Materials Chemistry A* 9, no. 1 (2021): 413–422, https://doi.org/10.1039/d0ta08224d.

42. Y. Gong, R. Qiu, C. Niu, et al., "Ag Incorporation With Controlled Grain Growth Enables 12.5% Efficient Kesterite Solar Cell with Open Circuit Voltage Reached 64.2% Shockley–Queisser Limit," *Advanced Functional Materials* 31, no. 24 (2021): 2101927, https://doi.org/10.1002/adfm.202101927.

43. W. Xie, Q. Sun, Q. Yan, et al., "10.24% Efficiency of Flexible Cu2ZnSn(S,Se)4 Solar Cells by Pre-Evaporation Selenization Technique," *Small* 18, no. 22 (2022): 2201347, https://doi.org/10.1002/smll.202201347.

44. Y. Sun, S. Qin, D. Ding, et al., "Promoting Carrier Collection by DMF/DMSO Binary Solvent for Efficient Kesterite Solar Cells," *Chemical Engineering Journal* 455 (2023): 140596, https://doi.org/10.1016/j.cej.2022.140596.

45. Y. Cui, M. Wang, P. Dong, et al., "DMF-Based Large-Grain Spanning Cu2ZnSn(Sx,Se1-x)4 Device with a PCE of 11.76%," *Advanced Science* 9, no. 20 (2022): 2201241, https://doi.org/10.1002/advs.202201241.

46. H. Geng, M. Wang, S. Wang, et al., "Two-Step Cooling Strategy for Synergistic Control of CuZn and SnZn Defects Enabling 12.87% Efficiency (Ag,Cu)2ZnSn(S,Se)4 Solar Cells," *Advanced Functional Materials* 33, no. 3 (2023): 2210551, https://doi.org/10.1002/adfm.202210551.

47. M. Wang, H. Geng, J. Zhu, et al., "Hyperactive Selenium Source Yields Kesterite Solar Cells With 12.86% Efficiency," *Advanced Functional Materials* 33, no. 44 (2023): 2307389, https://doi.org/10.1002/adfm.202307389.

48. X. Pan, X. Li, Y. Yang, et al., "12.3% Efficient Low Voc Loss Pure Sulfide Kesterite Solar Cells From DMSO Solution via Cadmium Alloying," *Advanced Energy Materials* 13, no. 38 (2023): 2301780, https://doi.org/10.1002/aenm.202301780.

49. Y. Qi, N. Wei, Y. Li, et al., "Passivating SnZn Defect and Optimizing Energy Level Alignment via Organic Silicon Salt Incorporation Toward Efficient Solution-Processed CZTSSe Solar Cells," *Advanced Functional Materials* 34, no. 12 (2024): 2308333, https://doi.org/10.1002/adfm.202308333.

50. J. Zhou, X. Xu, H. Wu, et al., "Control of the Phase Evolution of Kesterite by Tuning of the Selenium Partial Pressure for Solar Cells With 13.8% Certified Efficiency," *Nature Energy* 8, no. 5 (2023): 526–535, https://doi.org/10.1038/s41560-023-01251-6.

51. L. Cao, L. Wang, Z. Zhou, et al., "Modifying Surface Termination by Bidentate Chelating Strategy Enables 13.77% Efficient Kesterite Solar Cells," *Advanced Materials* 36, no. 16 (2024): 231918, https://doi.org/10.1002/adma.202311918.

52. Q. Zhou, Y. Sun, H. Li, et al., "Tailoring Addition Sequence of Metal Ions in Precursor Solution Drives Highly Efficient Kesterite Solar Cells," *Advanced Functional Materials* 34, no. 19 (2024): 2313301, https://doi.org/10.1002/adfm.202313301.

53. Y. Li, C. Cui, H. Wei, et al., "Suppressing Element Inhomogeneity Enables 14.9% Efficiency CZTSSe Solar Cells," *Advanced Materials* 36, no. 25 (2024): 2400138, https://doi.org/10.1002/adma.202400138.

54. Y. Gong, A. Jimenez-Arguijo, A. G. Medaille, et al., "Li-Doping and ag-Alloying Interplay Shows the Pathway for Kesterite Solar Cells With Efficiency Over 14%," *Advanced Functional Materials* 34 (2024): 2404669, https://doi.org/10.1002/adfm.202404669.

55. J. Wang, J. Shi, K. Yin, et al., "Pd (II)/Pd (IV) Redox Shuttle to Suppress Vacancy Defects at Grain Boundaries for Efficient Kesterite Solar Cells," *Nature Communications* 15, no. 1 (2024): 4344, https://doi.org/10.1038/s41467-024-48850-9.

56. Y. Zhao, X. Chen, S. Chen, et al., "Energy Band Alignment and Defect Synergistic Regulation Enable air-Solution-Processed Kesterite Solar Cells With the Lowest VOC Deficit," *Advanced Materials* (2024): 2409327, https://doi.org/10.1002/adma.202409327.

57. F. Ye, C. He, T. Wu, et al., "Sputtering Deposited and Energy Band Matched ZnSnN2 Buffer Layers for Highly Efficient cd-Free Cu2ZnSnS4 Solar Cells," *Advanced Functional Materials* 34, no. 38 (2024): 2402762, https://doi.org/10.1002/adfm.202402762.

58. J. J. S. Scragg, L. Choubrac, A. Lafond, T. Ericson, and C. Platzer-Björkman, "A low-Temperature Order-Disorder Transition in Cu2ZnSnS4 Thin Films," *Applied Physics Letters* 104, no. 4 (2014): 041911, https://doi.org/10.1063/1.4863685.

59. K. Sardashti, R. Haight, T. Gokmen, et al., "Impact of Nanoscale Elemental Distribution in High-Performance Kesterite Solar Cells," *Advanced Energy Materials* 5, no. 10 (2015): 1402180, https://doi.org/10.1002/aenm.201402180.

60. J. Fu, D. Kou, W. Zhou, et al., "Ag, Ge Dual-Gradient Substitution for Low-Energy Loss and High-Efficiency Kesterite Solar Cells," *Journal of Materials Chemistry A* 8, no. 42 (2020): 22292–22301, https://doi.org/10.1039/d0ta06318e.

61. G. Rey, T. P. Weiss, J. Sendler, et al., "Ordering Kesterite Improves Solar Cells: A low Temperature Post-Deposition Annealing Study," *Solar Energy Materials & Solar Cells* 151 (2016): 131–138, https://doi.org/10.1016/j.solmat.2016.02.014.

62. J. Kim, J. S. Jang, S. W. Shin, et al., "Novel mg- and Ga-Doped ZnO/Li-Doped Graphene Oxide Transparent Electrode/Electron-Transporting Layer Combinations for High-Performance Thin-Film Solar Cells," *Small* 19, no. 22 (2023): 2207966, https://doi.org/10.1002/smll.202207966.

63. C. Yan, J. Huang, K. Sun, et al., "Cu_2ZnSnS_4 Solar Cells With Over 10% Power Conversion Efficiency Enabled by Heterojunction Heat Treatment," *Nature Energy* 3, no. 9 (2018): 764–772, https://doi.org/10.1038/s41560-018-0206-0.

64. C. Niu, Y. Gong, R. Qiu, et al., "11.5% Efficient Cu2ZnSn(S,Se)4 Solar Cell Fabricated From DMF Molecular Solution," *Journal of Materials Chemistry A* 9, no. 22 (2021): 12981–12987, https://doi.org/10.1039/d1ta01871j.

65. M. Guc, S. Levcenko, I. V. Bodnar, et al., "Polarized Raman Scattering Study of Kesterite Type Cu2ZnSnS4 Single Crystals," *Scientific Reports* 6 (2016): 19414, https://doi.org/10.1038/srep19414.

66. D. Dumcenco and Y. S. Huang, "The Vibrational Properties Study of Kesterite Cu_2ZnSnS_4 Single Crystals by Using Polarization Dependent Raman Spectroscopy," *Optical Materials* 35, no. 3 (2013): 419–425, https://doi.org/10.1016/j.optmat.2012.09.031.

67. M. Y. Valakh, O. F. Kolomys, S. S. Ponomaryov, et al., "Raman Scattering and Disorder Effect in Cu2ZnSnS4," *Physica Status Solidi Rapid Research Letters* 7, no. 4 (2013): 258–261, https://doi.org/10.1002/pssr.201307073.

68. M. Altosaar, J. Raudoja, K. Timmo, et al., "Cu2Zn1-XCdXSn (Se1-YSy)4 Solid Solutions as Absorber Materials for Solar Cells," *Physica Status Solidi A: Applications and Material Science* 205, no. 1 (2008): 167–170, https://doi.org/10.1002/pssa.200776839.

69. H. Yoo and J. Kim, "Growth of Cu2ZnSnS4 Thin Films Using Sulfurization of Stacked Metallic Films," *Thin Solid Films* 518, no. 22 (2010): 6567–6572, https://doi.org/10.1016/j.tsf.2010.03.058.

70. M. Dimitrievska, A. Fairbrother, X. Fontané, et al., "Multiwavelength Excitation Raman Scattering Study of Polycrystalline Kesterite Cu_2ZnSnS_4 Thin Films," *Applied Physics Letters* 104, no. 2 (2014): 021901, https://doi.org/10.1063/1.4861593.

71. M. Dimitrievska, A. Fairbrother, A. Pérez-Rodríguez, E. Saucedo, and V. Izquierdo-Roca, "Raman Scattering Crystalline Assessment of Polycrystalline Cu_2ZnSnS_4 Thin Films for Sustainable Photovoltaic Technologies: Phonon Confinement Model," *Acta Materialia* 70 (2014): 272–280, https://doi.org/10.1016/j.actamat.2014.02.035.

72. P. A. Fernandes, P. M. P. Salomé, and A. F. Da Cunha, "Study of Polycrystalline Cu_2ZnSnS_4 Films by Raman Scattering," *Journal of Alloys and Compounds* 509, no. 28 (2011): 7600–7606, https://doi.org/10.1016/j.jallcom.2011.04.097.

73. W. Wang, H. Shen, L. H. Wong, Z. Su, H. Yao, and Y. Li, "A 4.92% Efficiency Cu2ZnSnS4 Solar Cell From Nanoparticle ink and Molecular Solution," *RSC Advances* 6, no. 59 (2016): 54049–54053, https://doi.org/10.1039/c6ra08604g.

74. J. He, L. Sun, S. Chen, Y. Chen, P. Yang, and J. Chu, "Composition Dependence of Structure and Optical Properties of Cu2ZnSn(S,Se)4 Solid Solutions: An Experimental Study," *Journal of Alloys and Compounds* 511, no. 1 (2012): 129–132, https://doi.org/10.1016/j.jallcom.2011.08.099.

75. X. Fontané, V. Izquierdo-Roca, E. Saucedo, et al., "Vibrational Properties of Stannite and Kesterite Type Compounds: Raman Scattering Analysis of Cu2(Fe,Zn)SnS4," *Journal of Alloys and Compounds* 539 (2012): 190–194, https://doi.org/10.1016/j.jallcom.2012.06.042.

76. M. C. Johnson, C. Wrasman, X. Zhang, M. Manno, C. Leighton, and E. S. Aydil, "Self-Regulation of cu/Sn Ratio in the Synthesis of Cu2ZnSnS4 Films," *Chemistry of Materials* 27, no. 7 (2015): 2507–2514, https://doi.org/10.1021/acs.chemmater.5b00108.

77. R. Caballero, E. Garcia-Llamas, J. M. Merino, et al., "Non-Stoichiometry Effect and Disorder in Cu_2ZnSnS_4 Thin Films Obtained by Flash Evaporation: Raman Scattering Investigation," *Acta Materialia* 65 (2014): 412–417, https://doi.org/10.1016/j.actamat.2013.11.010.

78. M. Kumar, A. Dubey, N. Adhikari, S. Venkatesan, and Q. Qiao, "Strategic Review of Secondary Phases, Defects and Defect-Complexes in Kesterite CZTS-Se Solar Cells," *Energy & Environmental Science* 8, no. 11 (2015): 3134–3159, https://doi.org/10.1039/c5ee02153g.

79. A. Nagoya, R. Asahi, R. Wahl, and G. Kresse, "Defect Formation and Phase Stability of Cu2ZnSnS4 Photovoltaic Material," *Physical Review B: Condensed Matter and Materials Physics* 81, no. 11 (2010): 113202, https://doi.org/10.1103/PhysRevB.81.113202.

80. V. Pakštas, G. Grincienė, A. Selskis, et al., "Improvement of CZTSSe Film Quality and Superstrate Solar Cell Performance Through Optimized Post-Deposition Annealing," *Scientific Reports* 12, no. 1 (2022): 16170, https://doi.org/10.1038/s41598-022-20670-1.

81. H. Wei, Y. Li, C. Cui, et al., "Defect Suppression for High-Efficiency Kesterite CZTSSe Solar Cells: Advances and Prospects," *Chemical Engineering Journal* 462 (2023): 142121, https://doi.org/10.1016/j.cej.2023.142121.

82. G. Ren, D. Zhuang, M. Zhao, et al., "CZTSSe Solar Cell With an Efficiency of 10.19% Based on Absorbers With Homogeneous Composition and Structure Using a Novel two-Step Annealing Process," *Solar Energy* 207 (2020): 651–658, https://doi.org/10.1016/j.solener.2020.07.016.

83. X. Zhao, Y. Pan, W. Chen, et al., "Insights Into the Efficiency Improvement for CZTSSe Solar Cells With Over 12% Efficiency via Ga Incorporation," *Advanced Functional Materials* 33, no. 29 (2023): 2301377, https://doi.org/10.1002/adfm.202301377.

84. M. Minbashi, A. Ghobadi, E. Yazdani, A. Ahmadkhan Kordbacheh, and A. Hajjiah, "Efficiency Enhancement of CZTSSe Solar Cells via Screening the Absorber Layer by Examining of Different Possible Defects," *Scientific Reports* 10, no. 1 (2020): 21813, https://doi.org/10.1038/s41598-020-75686-2.

85. C. Tamin, D. Chaumont, O. Heintz, A. Leray, and M. Adnane, "Improvement of Hetero-Interface Engineering by Partial Substitution of Zn in Cu2ZnSnS4-Based Solar Cells," *EPJ Photovoltaics* 13 (2022): 24, https://doi.org/10.1051/epjpv/2022022.

86. T. Minemoto, Y. Hashimoto, T. Satoh, T. Negami, H. Takakura, and Y. Hamakawa, "Cu (In,Ga)Se2 Solar Cells With Controlled Conduction Band Offset of Window/Cu (In,Ga)Se2 Layers," *Journal of Applied Physics* 89, no. 12 (2001): 8327–8330, https://doi.org/10.1063/1.1366655.

87. R. Haight, A. Barkhouse, O. Gunawan, et al., "Band Alignment at the Cu2ZnSn(SxSe1-x)4/CdS Interface," *Applied Physics Letters* 98, no. 25 (2011): 253502, https://doi.org/10.1063/1.3600776.

88. S. Y. Kim, J. Lee, D. H. Son, et al., "Reducing Carrier Recombination Loss by Suppressing Sn Loss and Defect Formation via Ag Doping in $Cu_2ZnSn(S,Se)_4$ Solar Cells," *Energy & Environmental Science* 2 (2024): 8609–8620, https://doi.org/10.1039/d4ee02485k.

89. T. K. Todorov, J. Tang, S. Bag, et al., "Beyond 11% Effi Ciency: Characteristics of State-of-the-Art Cu2ZnSn(S,Se)4 Solar Cells," *Advanced Energy Materials* 3, no. 1 (2013): 34–38, https://doi.org/10.1002/aenm.201200348.

90. M. Courel, A. Martinez-Ayala, T. G. Sanchez, et al., "Impact of Cd Concentrations on the Physical Properties of $Cu_2(Cd_xZn_{1-x})SnS_4$ Thin Films," *Superlattices and Microstructures* 122 (2018): 324–335, https://doi.org/10.1016/j.spmi.2018.07.032.

91. Y. E. Romanyuk, S. G. Haass, S. Giraldo, et al., "Doping and Alloying of Kesterites," *Journal of Physics: Energy* 1, no. 4 (2019): 044004, https://doi.org/10.1088/2515-7655/ab23bc.

92. N. J. Carter, C. J. Hages, J. E. Moore, et al., "Analysis of Temperature-Dependent Current-Voltage Characteristics for CIGSSe and CZTSSe Thin Film Solar Cells From Nanocrystal Inks," *2013 IEEE 39th Photovoltaic Specialists Conference (PVSC)* (2013): 3062–3065, https://doi.org/10.1109/PVSC.2013.6745107.

93. M. Kauk-Kuusik, K. Timmo, K. Muska, et al., "Reduced Recombination Through CZTS/CdS Interface Engineering in Monograin Layer Solar Cells," *Journal of Physics: Energy* 4, no. 2 (2022): 024007, https://doi.org/10.1088/2515-7655/ac618d.

94. Z. Yu, C. Li, S. Chen, et al., "Unveiling the Selenization Reaction Mechanisms in Ambient Air-Processed Highly Efficient Kesterite Solar Cells," *Advanced Energy Materials* 13, no. 19 (2023): 2300521, https://doi.org/10.1002/aenm.202300521.

95. B. Vermang, Y. Ren, O. Donzel-Gargand, et al., "Rear Surface Optimization of CZTS Solar Cells by use of a Passivation Layer With Nanosized Point Openings," *IEEE Journal of Photovoltaics* 6, no. 1 (2016): 332–336, https://doi.org/10.1109/JPHOTOV.2015.2496864.

96. J. J. Scragg, T. Kubart, J. T. Wätjen, T. Ericson, M. K. Linnarsson, and C. Platzer-Björkman, "Effects of Back Contact Instability on Cu2ZnSnS4 Devices and Processes," *Chemistry of Materials* 25, no. 15 (2013): 3162–3171, https://doi.org/10.1021/cm4015223.

97. F. Liu, J. Huang, K. Sun, et al., "Beyond 8% Ultrathin Kesterite Cu_2ZnSnS_4 Solar Cells by Interface Reaction Route Controlling and Self-Organized Nanopattern at the Back Contact," *NPG Asia Materials* 9, no. 7 (2017): e401, https://doi.org/10.1038/am.2017.103.

Supporting Information

Additional supporting information can be found online in the Supporting Information section.